Supporting Information

OER-Highly-Active Encapsulant to Improve the Electrochemical Anticorrosion of Fe-N-C for Ultralong-Lifespan and High-Rate Rechargeable Zinc-Air Batteries

Jiale Li,[a] Niu Huang,[a,*] Minghui Lv,[a] Na Su,[c] Chao Li,[a] Yingping Huang,[a] Yongye Wang,[a] Yong Zheng,[a] Wei Liu,[a] Tianyi Ma,[b,*] Liqun Ye[a,*]

[*] Corresponding author's E-mail addresses: huangliu.ysxf@163.com; tianyi.ma@rmit.edu.au; lqye@ctgu.edu.cn.

[a] *College of Materials and Chemical Engineering, Key Laboratory of Inorganic Nonmetallic Crystalline and Energy Conversion Materials, China Three Gorges University, Yichang 443002, China.*

[b] *School of Science, RMIT University, Melbourne, VIC 3000, Australia.*

[c] *School of New Energy and Materials, Southwest Petroleum University, Chengdu 610500, China.*

Experimental Section

✧ Materials

Ferrous citrate ($C_6H_8FeO_7$), nickel chloride hexahydrate ($NiCl_2 \cdot 6H_2O$), urea, dopamine hydrochloride (DA), dicyandiamide (DCA), hexadecyl trimethyl ammonium bromide (CTAB), terephthalic acid (PTA), 20% Pt/C (Sigma-Aldrich No. 738549) and Nafion®117 solution (5%, Sigma-Aldrich) are analytically pure. Hydrogen peroxide (H_2O_2, 35 wt.%) was purchased from Thermo Fisher Scientific. Horseradish peroxidase (HRP) was purchased from Shanghai Aladdin Bio-Chem Technnology Co., Ltd. HRP was a lyophilized powder, with a purity of RZ: >2.5 and activity: >200 units/mg. Carbon cloth (CC, HCP330N) was produced in Shanghai Hesen Electric Co., Ltd. The carbon cloths were treated with piranha water for 24 h to enhance their hydrophilization. Piranha water was made of concentrated sulfuric acid and hydrogen peroxide with a volume ratio of 7:3. Deionized water (DI, 18.25 MΩ) was obtained from a Millipore Milli-Q water purification system.

✧ Catalyst Syntheses

1. Syntheses of Fe-NCNT

Fe-NCNT@NiFe-LDH was prepared by a chemical bath deposition (CBD) method and a chemical vapor deposition (CVD) method. First, $C_6H_8FeO_7$ of 0.7378 g and urea of 2.667 g were dissolved in 40 mL DI water. Then, the mixed liquid was placed in cuvette with a piece of CC immersed into, which was kept at 95℃ for 3 h. After that, the CC piece with Fe-precursor grown on was clipped out, washed by DI water for

several times, and dried for use. Second, DA of 0.4 mg/mL was dissolved in Tris solution (pH = 8.5). Then, the above CC piece was soaked in the homogeneous solution at room temperature for 24 h. After that, polydopamine (PDA) was coated on the Fe-precursor. Third, the Fe-NCNT catalyst was prepared by a CVD method. That is, the above CC/Fe-precursor@PDA as a catalyst for catalyzing the growth of NCNTs was put in the middle of a quartz tube, DCA of 1 g served as solid source was put near the inlet port, and the reaction was processed at 350℃ for 1 h and then heated up to 900℃ for 2 h with Ar as the carrier gas.

2. Synthesis of NiFe-LDH

$NiCl_2 \cdot 6H_2O$ of 0.71307 g, $C_6H_8FeO_7$ of 0.2459 g, urea of 2.667 g, and CTAB of 0.7289 g were dissolved in 40 mL DI water. Then, the mixed liquid was placed in cuvette with a piece of CC immersed into, which was kept at 95℃ for 3 h. After that, NiFe-LDH was grown on the CC substrate.

3. Syntheses of Fe-NCNT@NiFe-LDH

$NiCl_2 \cdot 6H_2O$ of 0.71307 g, $C_6H_8FeO_7$ of 0.2459 g, urea of 2.667 g, and CTAB of 0.7289 g were dissolved in 40 mL DI water. Then, the mixed liquid was placed in cuvette with Fe-NCNT immersed into, which was kept at 95℃ for 3 h. After that, NiFe-LDH was grown on the NCNTs of the Fe-NCNT, integrated as Fe-NCNT@NiFe-LDH.

✧ Material Characterization

X-ray powder diffraction (XRD) was performed on a Rigaku Ultima IV diffractometer with an X-ray generator power of 3 KW (Cu-K_α radiation). The

microstructures and morphologies of catalysts were characterized by field-emission scanning electron microscope (FESEM, JEOL, JSM-7500F) and transmission electron microscopy (TEM, FEI JEOL-2100F). The compositions and element states of catalysts were measured by X-ray photoelectron spectroscopy (XPS, Escalab 250Xi X-ray, Thermo Scientific).

✧ Reaction Mechanism

1. 4-electron oxygen reduction reaction (ORR)

It is widely acknowledged that ORR could be carried out via a 4-electron transfer pathway in alkaline solution. The detailed steps are as follows:

$$O_2 + 2H_2O + 4e^- \rightarrow OOH^* + H_2O + OH^- + 3e^- \quad (1)$$

$$OOH^* + H_2O + OH^- + 3e^- \rightarrow O^* + H_2O + 2OH^- + 2e^- \quad (2)$$

$$O^* + H_2O + 2OH^- + 2e^- \rightarrow OH^* + 3OH^- + e^- \quad (3)$$

$$OH^* + 3OH^- + e^- \rightarrow 4OH^- \quad (4)$$

where * represents on surface active sites.

Alternatively, ORR could be carried out via another 4-electron transfer pathway in alkaline solution via 2-electron transfer process from O_2 to H_2O_2 plus 2-electron transfer process from H_2O_2 to OH^-. The detailed steps are as follows:

2-electron transfer process from O_2 to H_2O_2

$$O_2 + 2H_2O + 4e^- \rightarrow OOH^* + H_2O + OH^- + 3e^- \quad (5)$$

$$OOH^* + H_2O + OH^- + 3e^- \rightarrow H_2O_2^* + 2OH^- + 2e^- \quad (6)$$

2-electron transfer process from H_2O_2 to OH^-

$$H_2O_2{*} + 2OH^- + 2e^- \rightarrow OH{*} + 3OH^- + e^- \quad (7)$$

$$OH{*} + 3OH^- + e^- \rightarrow 4OH^- \quad (8)$$

Notably, $H_2O_2{*}$ represents the hydrogen peroxide molecule is adsorbed on catalyst surface. Here H_2O_2 acts as an ORR intermediator. Intermediate H_2O_2 may pose threats to Fe-N-C catalyst structure via corrosion through Fenton and Fenton-like reactions.

2. Generation of hydrogen peroxide

The ORR reaction also could be carried out via a 2-electron transfer process, which is accompanied by the production of H_2O_2 in alkaline solution. The reaction steps are suggested below:

$$O_2 + 2H_2O + 2e^- \rightarrow OOH{*} + H_2O + OH^- + e^- \quad (9)$$

$$OOH{*} + H_2O + e^- \rightarrow H_2O_2 + OH^- \quad (10)$$

Notably, H_2O_2 represents the hydrogen peroxide molecule is dissolved into aqueous electrolyte. Here H_2O_2 acts as the ORR byproduct. Generation of byproduct H_2O_2 means lower current density, which will in turn cut down the output power density of the Zn-air battery in discharging process. Besides, H_2O_2 is detrimental to Fe-N-C catalyst stability.

3. Decomposition of byproduct H_2O_2 involving •OH radicals[1, 2]

H_2O_2 could be decomposed to •OH radicals under some surroundings through Fenton or Fenton-like reactions. The Fenton reactions occur as follows:

$$Fe^{2+} + H_2O_2 \leftrightarrow Fe^{3+} + {\bullet}OH + OH^- \quad (11)$$

The reduction of Fe^{3+} is achieved as follows:

$$Fe^{3+} + H_2O_2 + OH^- \leftrightarrow Fe^{2+} + {\bullet}OOH + H_2O \quad (12)$$

$$Fe^{3+} + \bullet OOH + OH^- \leftrightarrow Fe^{2+} + O_2 + H_2O \quad (13)$$

$$2Fe^{3+} + H_2O_2 + 2OH^- \leftrightarrow 2Fe^{2+} + O_2 + 2H_2O \quad (14)$$

•OH radicals as a highly reactive oxygen group can damage durability via two pathways, one involves the conversion of the carbon substrate to CO_2, resulting in the stripping of the metal active center, another is the establishment of oxygen functional groups within the catalyst, which will critically reduce the catalytic performance of the catalyst.

4. Consumption of byproduct H_2O_2 without radicals[3]

To eliminate the effect of •OH radicals on the stability of the catalyst, H_2O_2 could be consumed via electrochemical pathways. There are two types of electrochemical reaction pathways that are peroxide reduction reaction (PRR) and peroxide oxidation reaction (POR) with the following equations:

PRR: $H_2O_2 + 2e^- \leftrightarrow 2OH^-$ (15)

POR: $H_2O_2 - 2e^- + 2OH^- \leftrightarrow 2H_2O + O_2$ (16)

In addition, H_2O_2 could be consumed via an important non-electrochemical pathway, that is disproportionation with the following equation:[4]

$$2H_2O_2 \leftrightarrow O_2 + 2H_2O \quad (17)$$

✧ Measurements

1. Electrochemical tests on electrodes

Electrochemical measurements were performed via electrochemical workstations (CHI760E, Chenhua shanghai). Except specifically stated, all linear voltammetry curves (LSV) were corrected via a scan rate of 5 mV s^{-1} and with 95%-*iR* compensation

in a three-electrode system, which comprises of a counter electrode (carbon rod), a reference electrode (Hg/HgO electrode), and a working electrode. Electrochemical impedance spectroscopy (EIS) was carried out between 0.01 Hz and 100 kHz (AC voltage with 5 mV). The electrochemical active surface area (ECSA) of the catalysts were determined by calculating its bilayer capacitance (C_{dl}). The C_{dl} value was obtained via CV curves measured in non-Faradic potential ranges with different scan rates. The calculation formula was as $C_{dl} = \Delta j/2v$, where Δj is defined as the difference between the current densities at the middle potential of each curves and v corresponds to scan rates.

2. Gas diffusion electrode (GDE) test

The ORR activities of Fe-NCNT@NiFe-LDH, Fe-NCNT, NiFe-LDH, and Pt/C were tested via a gas diffusion electrode (GDE), which supports an advanced three-phase (gas-liquid-solid) interface on the catalyst surface.[5-7] Because of the low saturated O_2 concentration in aqueous electrolyte, the mass transport limitation widely exists in LSV, rotating disk electrode (RDE), and rotating ring disk electrode (RRDE) tests. However, through the design on gas flow, the mass transport limitation could be well avoided to achieve larger ORR current density.

The GDE test as well employed the three-electrode test system, with the catalyst as working electrode, the carbon rod as counter electrode, and Hg/HgO electrode as reference electrode, with the 1M KOH aqueous electrolyte saturated by O_2. The structure of GDE is schematically shown in Figure S10.

The method to make the catalyst-loaded working electrode was as follows. Fe-

NCNT@NiFe-LDH, Fe-NCNT, and NiFe-LDH of 1 cm^2 geometric area (They are in-situ grown on CC) were respectively ground to fine powder in an agate mortar and to prepare slurry by adding drops of anhydrous ethanol and 30 μL of Nafion (for each catalyst). The slurry was then uniformly dropped on a piece of hydrophobic carbon cloth with the catalyst centered at an area of 1 cm^2, and then dried at 60℃ in air. For Pt/C, commercial 20% Pt/C of 5 mg and carbon cloth of 1 cm^2 (~ 10 mg) were used to prepare slurry, and otherwise synthetic conditions were identical.

3. Rotating ring disc electrode (RRDE) and rotating disc electrode (RDE) tests

ORR performance

To evaluate the ORR performances of catalysts in O_2-saturated 0.1 M KOH, RRDE (ALS, RRDE-3A) was carried out using the rotation speed of 1600 rpm. Fe-NCNT@NiFe-LDH, Fe-NCNT, NiFe-LDH, and Pt/C based slurries were respectively prepared via the same operations as used in GDE measurement. Each kind of slurry was carefully transformed onto the glassy carbon disc electrode of the RRDE. After drying at room temperature and in air, a uniform and dense film should be guaranteed on the surface of the disc electrode.

Electron transfer number (n) and hydrogen peroxide yield (H_2O_2%) were calculated according to the following two formulas:

$$\mathrm{n} = 4 \times \frac{I_D}{I_D + \frac{I_R}{N}} \tag{18}$$

$$H_2O_2\% = 200 \times \frac{\frac{I_R}{N}}{\frac{I_R}{N} + I_D} \tag{19}$$

where I_R and I_D were the ring and disk currents, N was the ring electrode collection

efficiency and was 0.4 here.

Peroxidase-coupled RRDE

To investigate the specific pathway of electron transfer, horseradish peroxidase was introduced to (partially) terminate the "2+2"-electron transfer pathway of ORR by capturing H_2O_2. The test conditions and electrode preparation were the same as for the RRDE test, except with 0.02 mg/mL horseradish peroxidase added into the O_2-saturated 0.1 M KOH aqueous electrolyte. HRP is a natural metalloenzyme extracted from the roots of the horseradish plant. HRP reacts with H_2O_2 to form compound I with a reaction rate coefficient of $1*10^7$ $M^{-1}s^{-1}$.[8] The capture mechanism of horseradish peroxidase on H_2O_2 is as follows.[9]

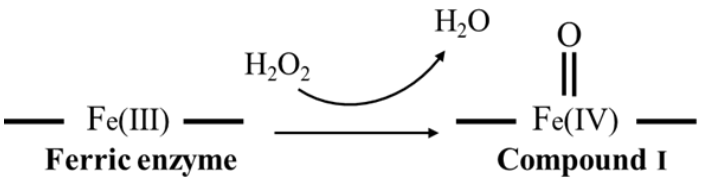

(20)

PRR and POR by RDE

The test conditions and electrode preparations were the same as for the RRDE test, except that 10 mM H_2O_2 was introduced and the electrolyte solution was saturated by N_2 in the tests. LSV curves for PRR performances were collected in the range from 1.0 V to 0.3 V vs RHE (in the negative potential direction), and LSV curves for POR performances were collected in the range from 0.9 V to 1.7 V vs RHE (in the positive potential direction).

4. Fluorescence test

Detection on •OH radical[10-12] was performed by using a fluorescence spectrophotometer (SHIMADZU, RF-6000A) with the excitation wavelength of 315 nm, the excitation bandwidth of 1.5 nm, and the wavelength range of 300 nm to 500 nm.

To probe if •OH radical could be generated without H_2O_2, the catalyst samples (Fe-NCNT@NiFe-LDH, Fe-NCNT, and NiFe-LDH) with 1 cm^2 geometric area were immersed into a solution of 20 mL consisting of 0.1 M KOH and 0.08 mg/mL PTA, respectively. After holding at 30 °C for 24 h, 3 mL solution was extracted out for fluorescence test. The corresponding result is shown in Figure 5g in the main body, where the sample marked "blank sample" represents no catalyst is introduced into the solution while other conditions are identical.

To probe if •OH radical was generated through Fenton reactions in ZABs, the catalyst samples with 1 cm^2 geometric area were immersed into a solution of 20 mL consisting of 0.1 M KOH and 0.08 mg/mL PTA, respectively. After ORR reaction at a constant potential of 0.5 V vs RHE for 3 h, 3 mL solution was extracted out for fluorescence test. The corresponding result is shown in Figure 5h in the main body.

Furthermore, to resemble byproduct H_2O_2 in high concentration, the catalyst samples with 1 cm^2 geometric area were immersed into a solution of 20 mL consisting of 0.1 M KOH, 0.08 mg/mL PTA and 10 mM H_2O_2, respectively. After holding at 30 °C for 24 h, 3 mL solution was extracted out for fluorescence test. The corresponding result is shown in Figure 5i in the main body, where the sample marked "blank sample"

represents no catalyst is introduced into the solution while other conditions are identical.

If there are •OH radicals, they will capture fast by PTA through the reaction as follows:

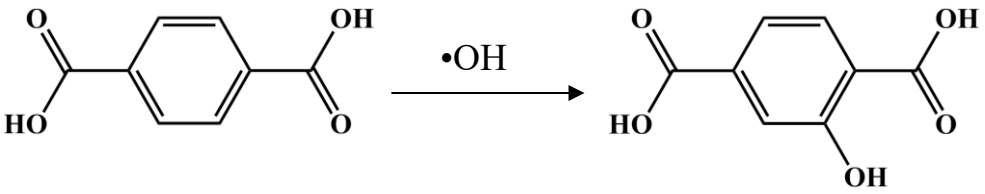

(21)

The generated 2-Hydroxy terephthalic acid has a fluorescent effect with the emission wavelength of ~ 425 nm.

5. H_2O_2 detection methods.

A phosphate buffer was prepared by dissolving 2.8756 g $K_2HPO_4 \cdot 3H_2O$ and 11.935 g KH_2PO_4 in 200 ml deionized water. Then prepared N, N-diethyl-1,4-phenylenediamine sulfate (DPD, 97%, Aldrich) and peroxidase (POD, horseradish, Aldrich) stock solutions. (Dissolve 0.1 g DPD in 10 ml 0.05 M H_2SO_4 solution and 10 mg POD in 10 ml deionized water.) During the experiment, take 2.5ml sample solution into a quartz tube each time, added 0.4 ml phosphate buffer and 50 μL POD solution in sequence. Liter and 50 microliters of DPD solution, mix well. Useing UV-2600 (Shanghai Tianmei Scientific Instrument Co., Ltd.) to measure absorbance at 552 nm. Calibrate the H_2O_2 concentration by diluting a 30% H_2O_2 stock solution.[13]

6. Off-line gas chromatography test

DI water of 4 mL were added to the bottom of a quartz reactor with the volume of 250 mL (PQ256, purchased from Beijing Perfect light Technology Co., Ltd., China). Fe-NCNT@NiFe-LDH and Fe-NCNT were then respectively immersed into the DI

water. And then, the reactor is sealed, and Ar gas was continuously introduced into the reactor for half an hour to remove the original oxygen from the system. After that, 50 μL H_2O_2 (35 wt.%) was added into the DI water, and simultaneously timing was begun. At 5, 9, 13, 17, 21, 25, and 29 min, 1 mL gas was extracted from the system at each time and used for analysis via gas chromatographs (GC9790II, FULI INSTRUMENTS).

7. Aqueous Zn-air battery (ZAB) assembly and performance measurements

CC/catalysts of 1 cm^2 geometric area were sandwiched by two pieces of nickel foam. And to enhance air diffusion, an air diffusion layer was made on the outward side of the air cathodes. The detail is as follows. A viscous slurry was prepared by adequately mixing 0.9 g carbon black, 3 mL isopropanol and 0.1 mL PTFE (10 wt% in DI water). Then, the slurry was applied evenly to one side of the sandwich (that is the outside of one piece of nickel foam) until every cavity was filled. And then the above sandwich was compressed tightly by using an even pressure of 3 MPa for 2 min. Finally, the excess slurry on the surface was scraped off by using a plastic or stainless-steel blade. The above electrodes were used as the air cathode, polished zinc foil was used as the anode, and a mixture of 6.0 M KOH + 0.2 M $Zn(CH_3COO)_2$ was used as the electrolyte. The structure of the assembled ZABs is schematically shown in Figure 6a in the main body.

All ZABs were measured in air conditions without pumping oxygen.

Figures and Discussion

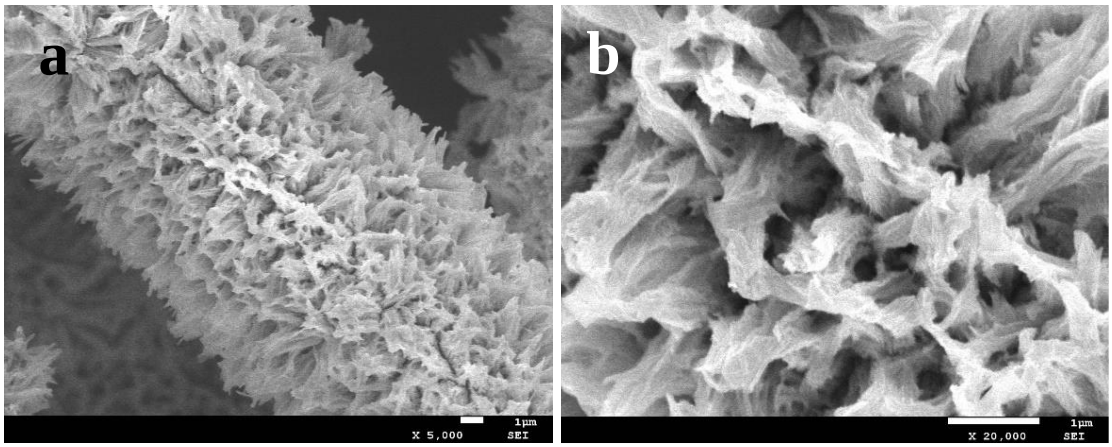

Figure S1. SEM images of FeOx(OH)y grown on the carbon fibers of CC.

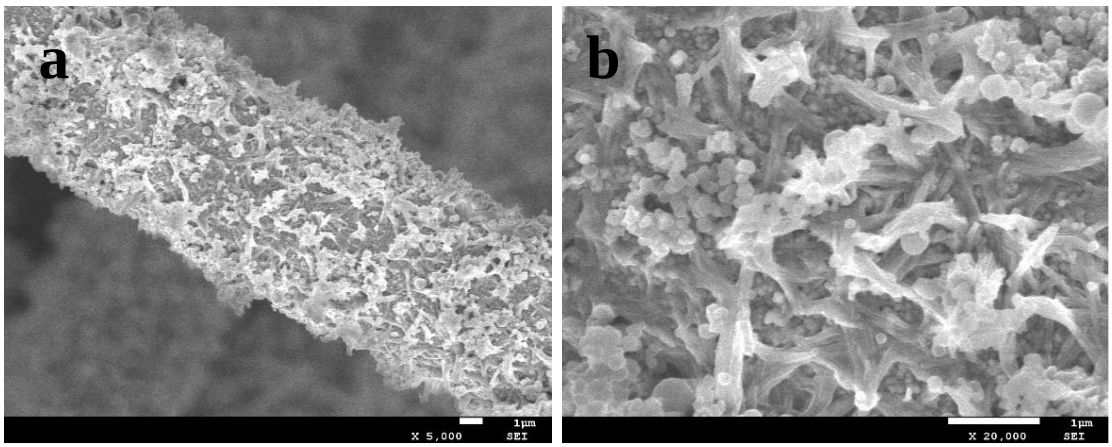

Figure S2. SEM images of FeOx(OH)y@PDA grown on the carbon fibers of CC.

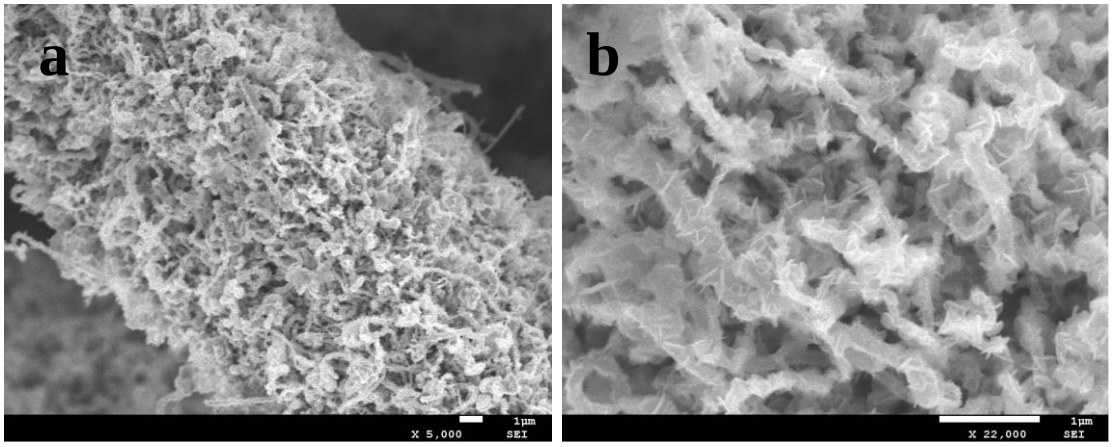

Figure S3. SEM images of Fe-NCNT@NiFe-LDH grown on the carbon fibers of CC, where NiFe-LDH is synthesized without CTAB addition.

As revealed in Figure S3, when CTAB was not added, the NiFe-LDH nanosheets on the surface of Fe-NCNT nanotubes were not uniformly distributed and had low coverage.

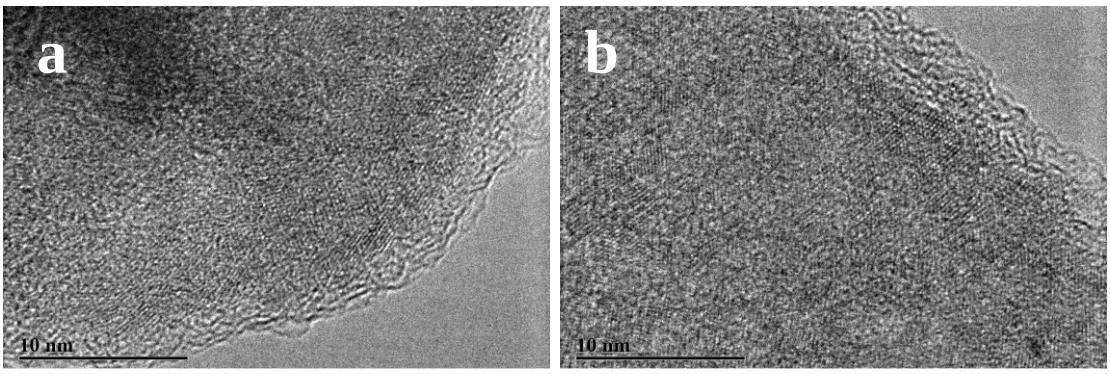

Figure S4. HRTEM images of NiFe-LDH of Fe-NCNT@NiFe-LDH.

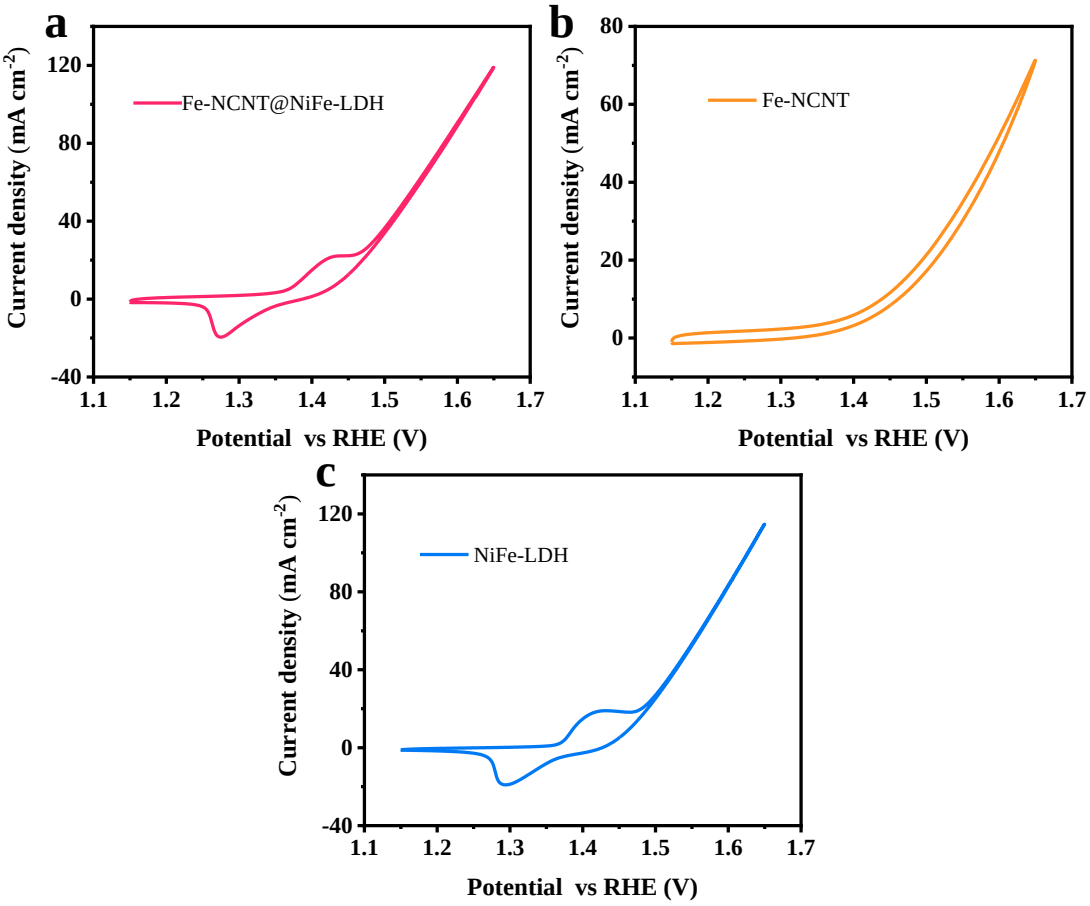

Figure S5. CV curves of (a) Fe-NCNT@NiFe-LDH, (b) Fe-NCNT, and (c) NiFe-LDH, measured in O_2-saturated 1 M KOH without *iR* compensation.

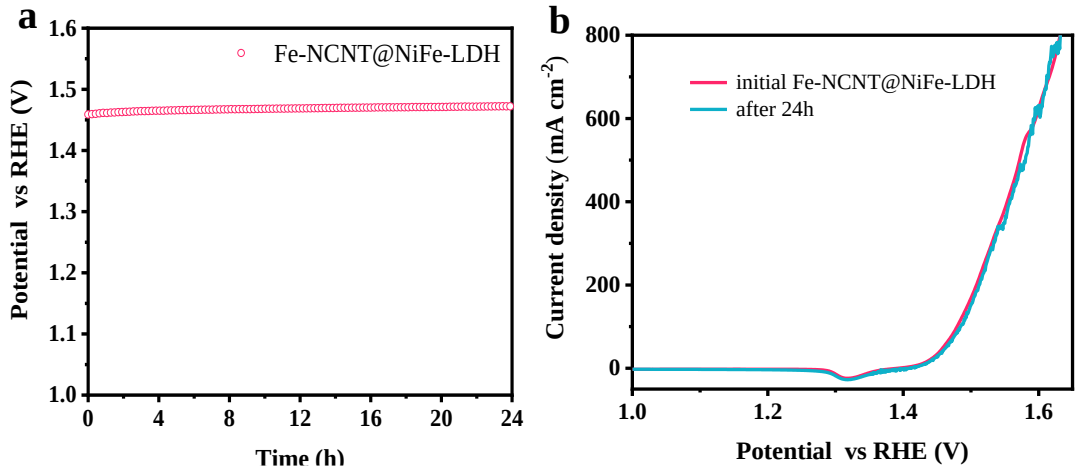

Figure S6. (a) Chronopotentiometric curve of Fe-NCNT@NiFe-LDH measured at a constant current density of 10 mA cm^{-2} for 24 h in O_2-saturated 1 M KOH electrolyte,

(b) LSV curves before and after the stability test.

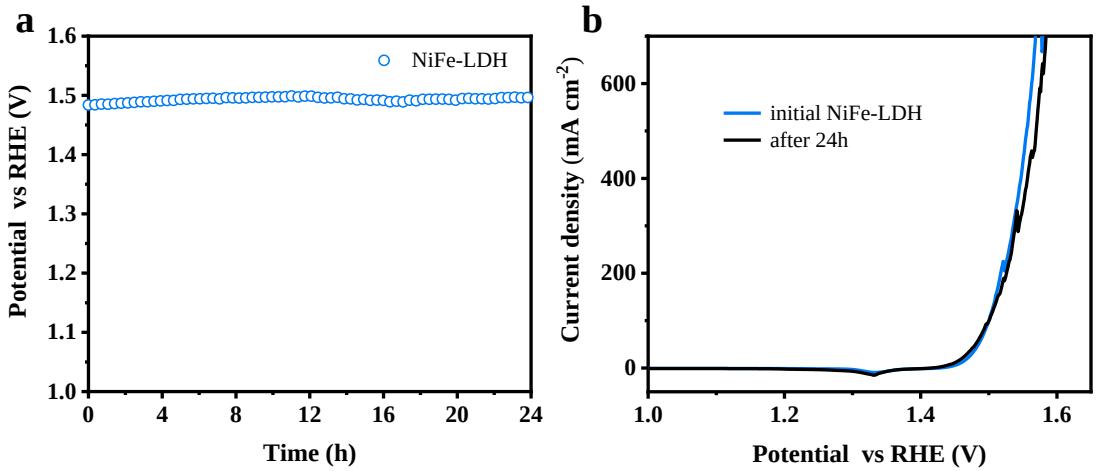

Figure S7. (a) Chronopotentiometric curve of NiFe-LDH measured at a constant current density of 10 mA cm^{-2} for 24 h in O_2-saturated 1 M KOH electrolyte, (b) LSV curves before and after the stability test.

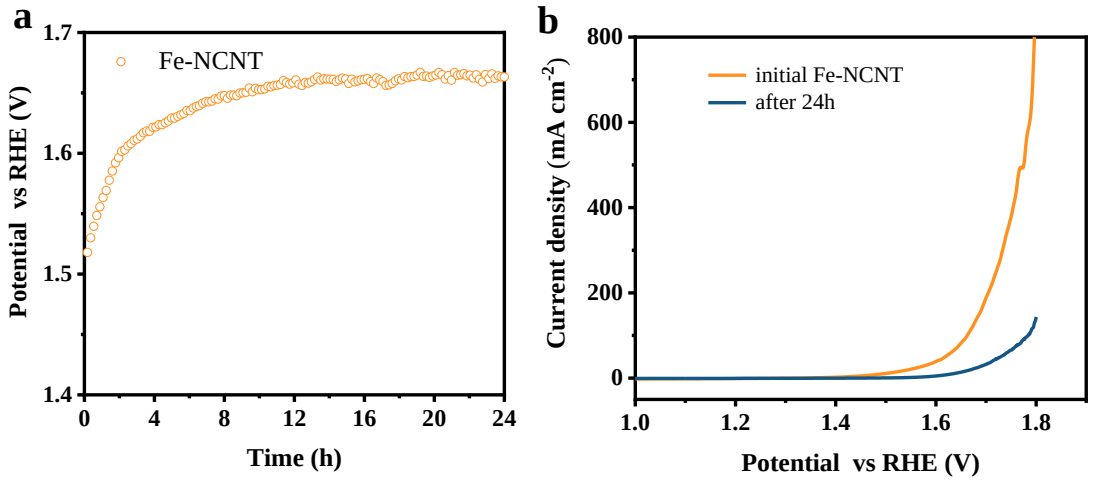

Figure S8. (a) Chronopotentiometric curve of Fe-NCNT measured at a constant current density of 10 mA cm^{-2} for 24 h in O_2-saturated 1 M KOH electrolyte, (b) LSV curves before and after the stability test.

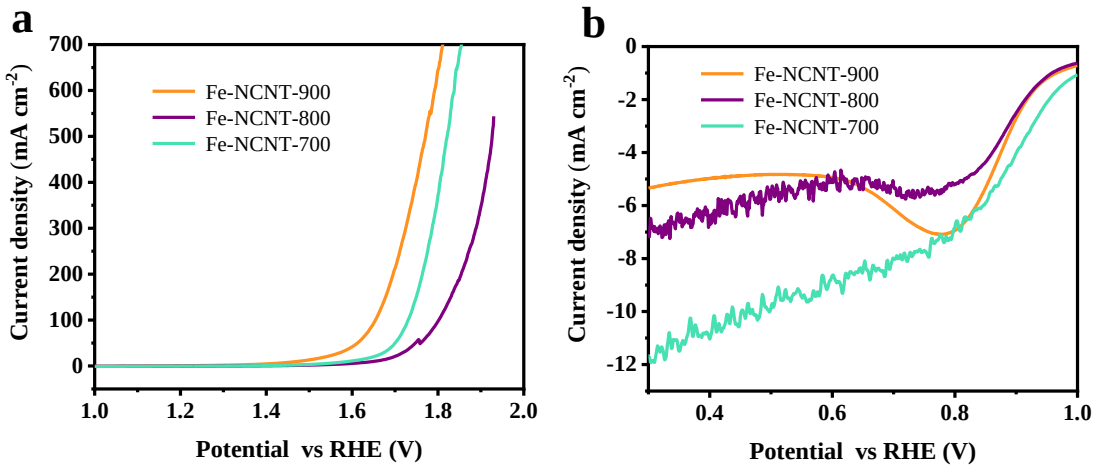

Figure S9. (a) OER-LSV curves and (b) ORR-LSV curves of Fe-NCNT-700, Fe-NCNT-800 and Fe-NCNT-900, measured in O_2-saturated 1 M KOH.

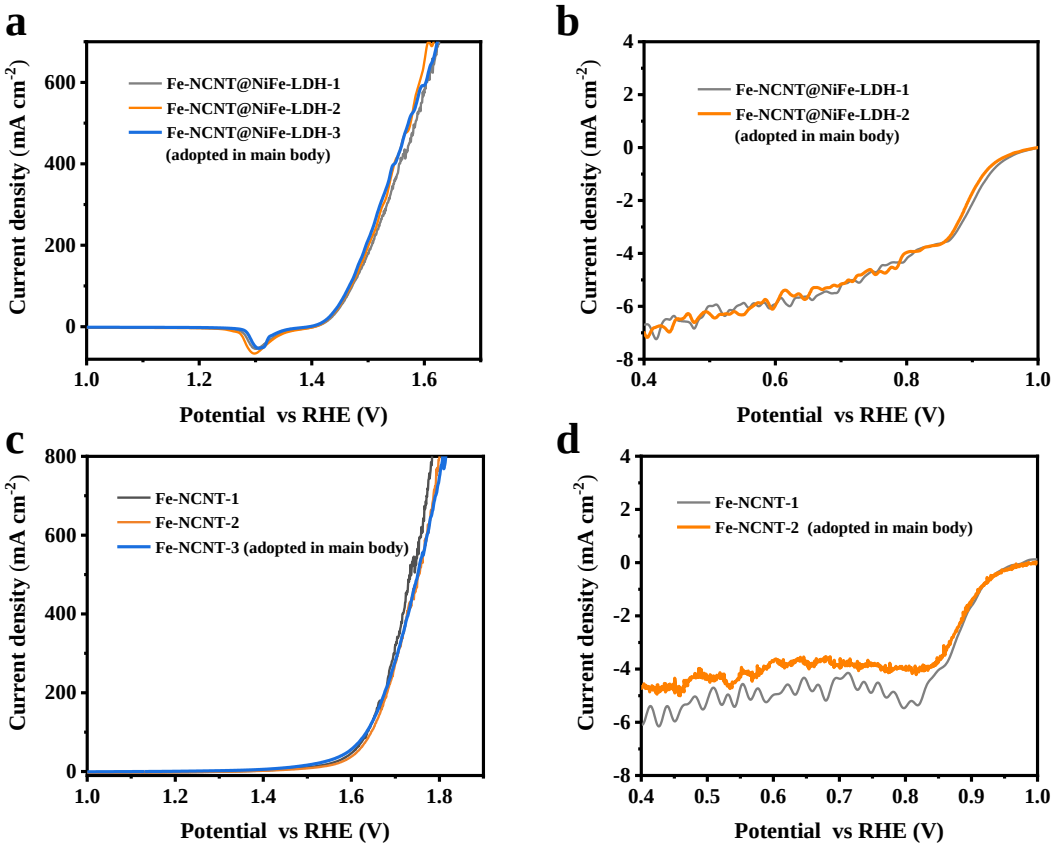

Figure S10. Reproducibility of Fe-NCNT@NiFe-LDH from different Batches: (a) OER at 1 M KOH and (b) ORR at 0.1 M KOH; Reproducibility of Fe-NCNT from

different Batches: (a) OER at 1 M KOH and (b) ORR at 0.1 M KOH.

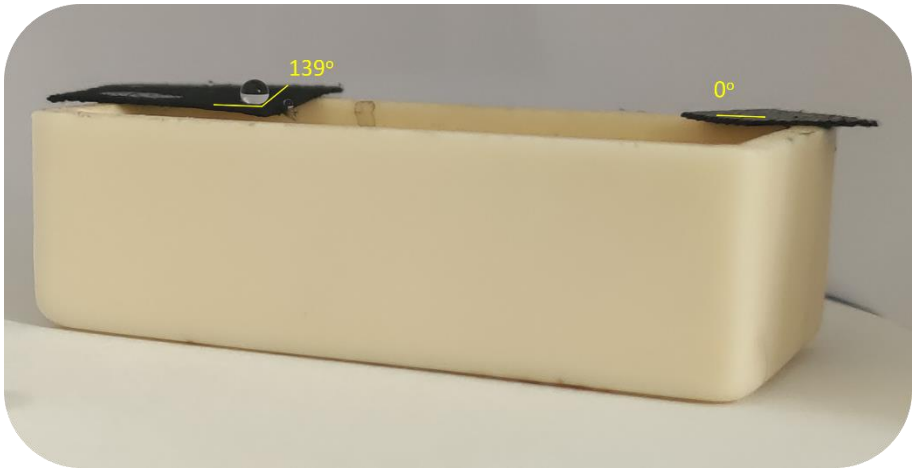

Figure S11. Contact angles of DI water on Fe-NCNT (in the left) and Fe-NCNT@NiFe-LDH (in the right).

Notes: Movies S1 (Hydrophilicity/hydrophobicity evaluation of Fe-NCNT) **and S2** (Hydrophilicity/hydrophobicity evaluation of Fe-NCNT@NiFe-LDH) are separately uploaded as MP4 files.

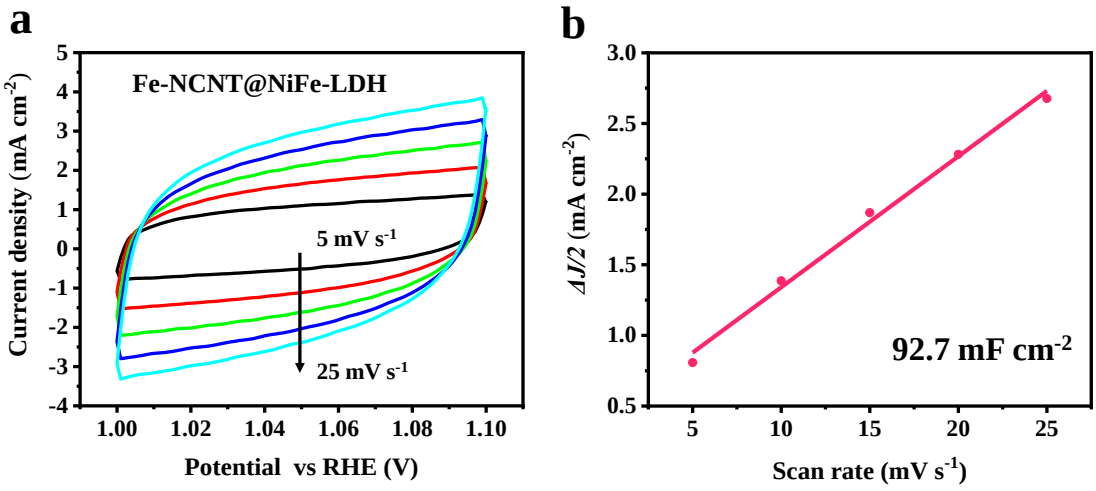

Figure S12. (a) CV curves of Fe-NCNT@NiFe-LDH at 5, 10, 15, 20, and 25 mV/s

scanning rates. (b) Correspondingly plot of the capacitive current as a function of the scan rate of the Fe-NCNT@NiFe-LDH.

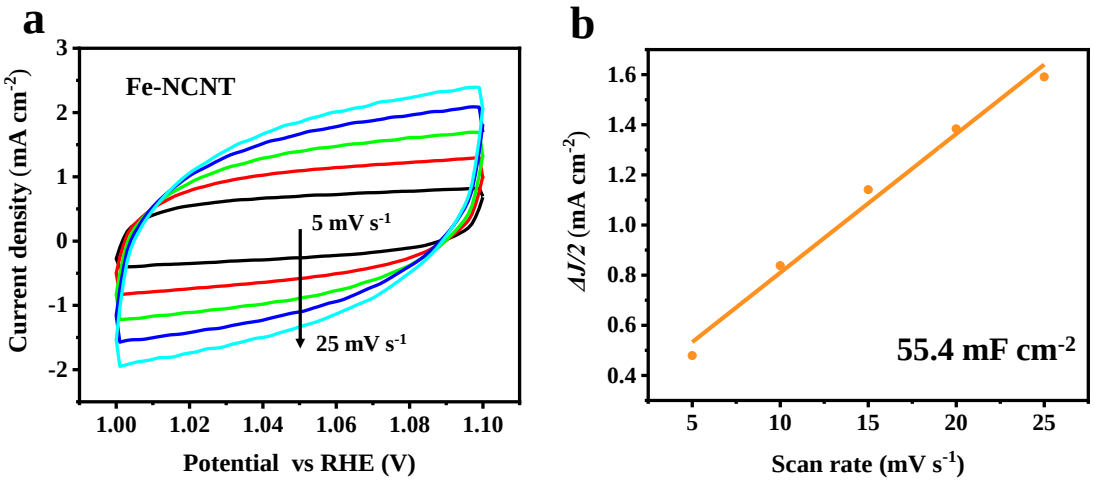

Figure S13. (a) CV curves of Fe-NCNT at 5, 10, 15, 20, and 25 mV/s scanning rates. (b) Correspondingly plot of the capacitive current as a function of the scan rate of the Fe-NCNT.

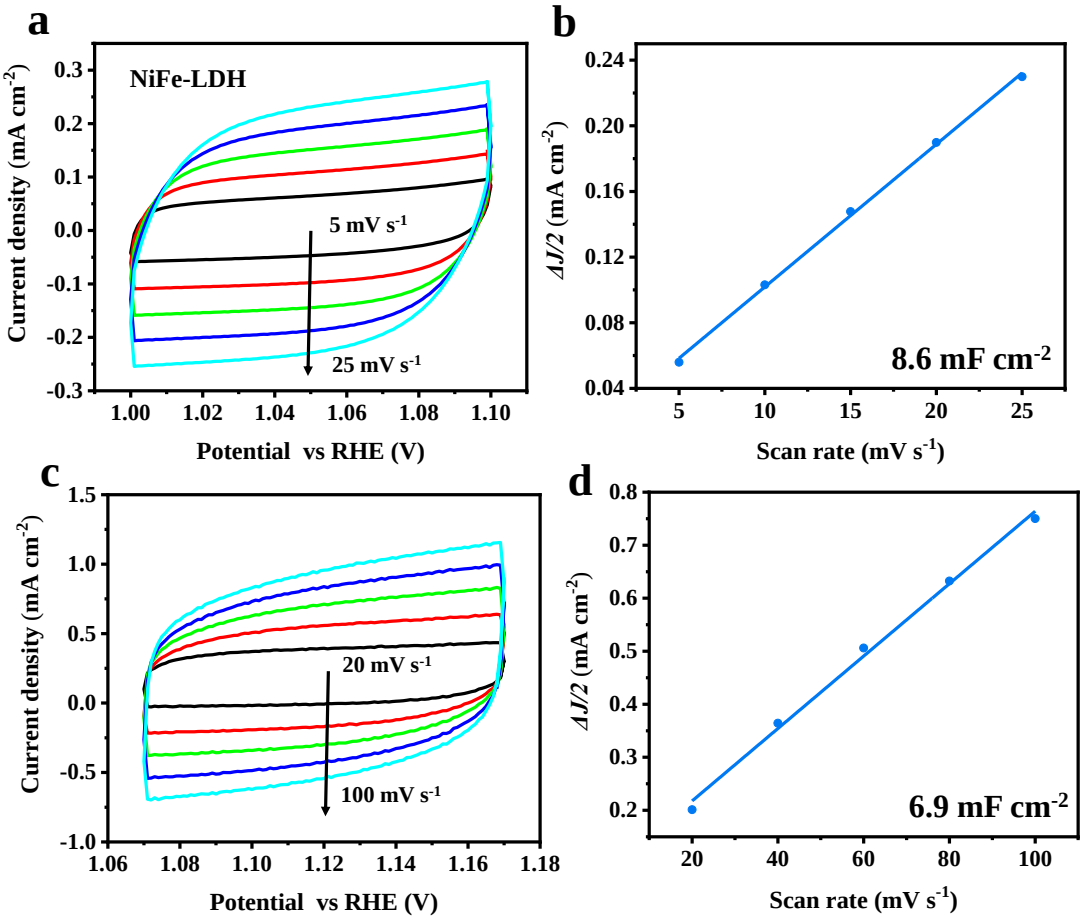

Figure S14. (a) CV curves of NiFe-LDH measured at 5, 10, 15, 20, and 25 mV/s scanning rates in potential range from 1.0 to 1.1 V vs. RHE. (b) Correspondingly plot of the capacitive current as a function of the scan rate of the Fe-NCNT@NiFe-LDH. (c) CV curves of NiFe-LDH measured at 20, 40, 60, 80, and 100 mV/s scanning rates in potential range from 1.07 to 1.17 V vs. RHE. (d) Correspondingly plot of the capacitive current as a function of the scan rate of the Fe-NCNT@NiFe-LDH.

Figures S11-13 show CV curves of Fe-NCNT@NiFe-LDH, Fe-NCNT, and NiFe-LDH measured at non-Faradic potential ranges. The electrochemical double-layer capacitance (C_{dl}) is calculated from the CV curves via different sweep speeds. As shown in Figures S10b, S11b, and S12b, the C_{dl} value of the Fe-NCNT@NiFe-LDH is 92.7

mF cm^{-2}, which is higher than the Fe-NCNT (55.4 mF cm^{-2}), and much larger than that of NiFe-LDH (6.9~8.6 mF cm^{-2}). The electrochemical active surface area (ECSA) of the catalysts are positively correlated with the value of C_{dl}. The C_{dl} trend clearly demonstrates that Fe-NCNT@NiFe-LDH has larger electrochemical active surface area per geometric area, superior to Fe-NCNT and NiFe-LDH. And the C_{dl} values of Fe-NCNT@NiFe-LDH and Fe-NCNT are almost 10 times of that of NiFe-LDH. The enhancement of ECSA of Fe-NCNT@NiFe-LDH probably originates from its uniform wrapping structure with thinner vertically grown NiFe-LDH nanosheets, facilitating to achieve high surface area and better mass accessibility.

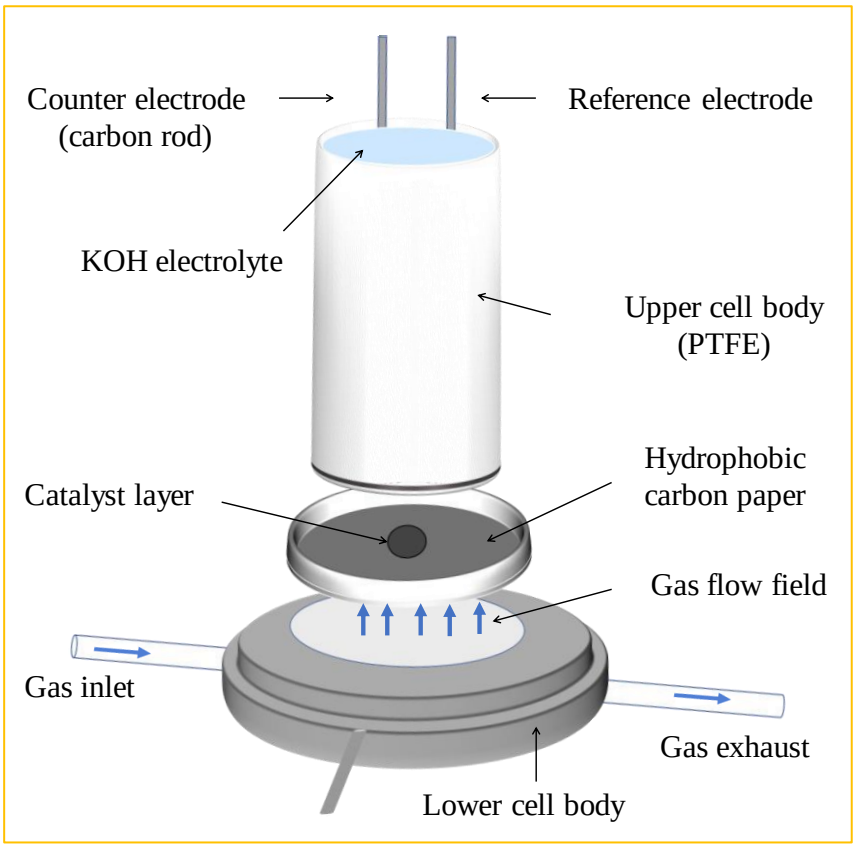

Figure S15. Schematic structure of GDE equipment.

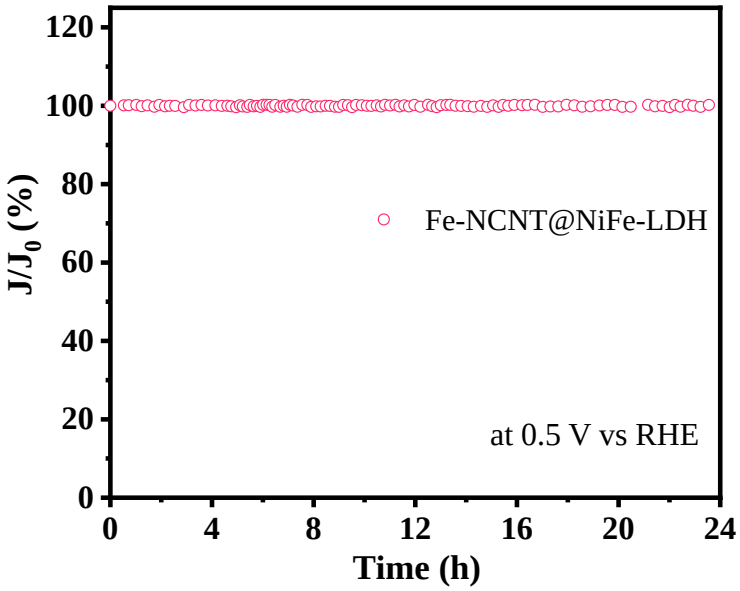

Figure S16. Durability test of Fe-NCNT@NiFe-LDH measured at constant potential of 0.5 V vs RHE.

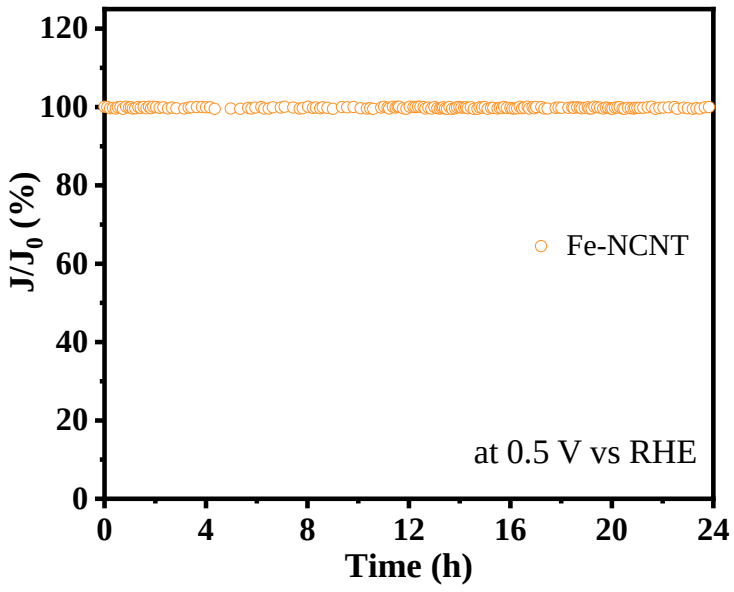

Figure S17. Durability test of Fe-NCNT measured at constant potential of 0.5 V vs RHE.

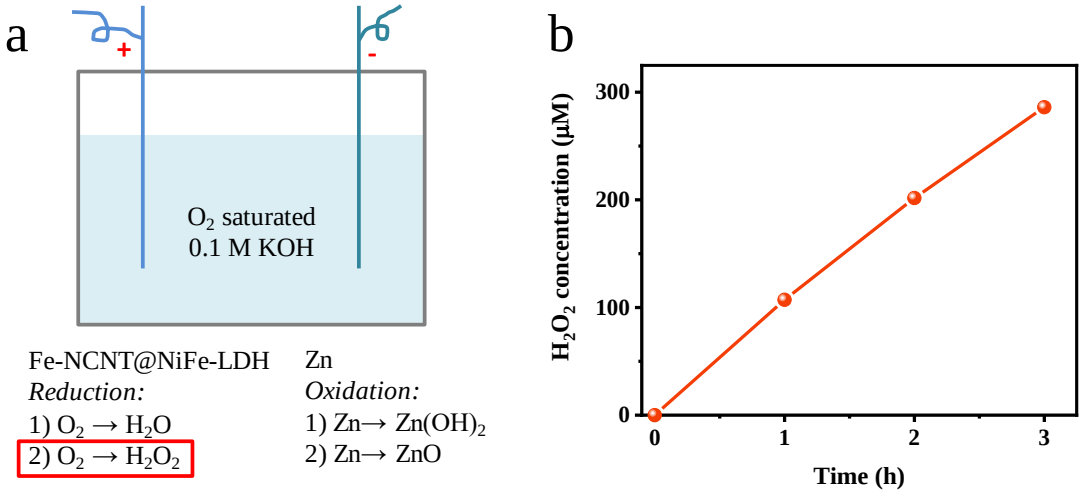

Figure S18. (a) A simulated Zn-air discharging battery and (b) The H_2O_2 accumulation along with discharging time. Conditions: The area of CFP/Fe-NCNT@NiFe-LDH is of 2 cm^2, the area of Zn plate is of 6 cm^2, the volume of the electrolyte is of 130 mL, and the discharging current is 10 mA.

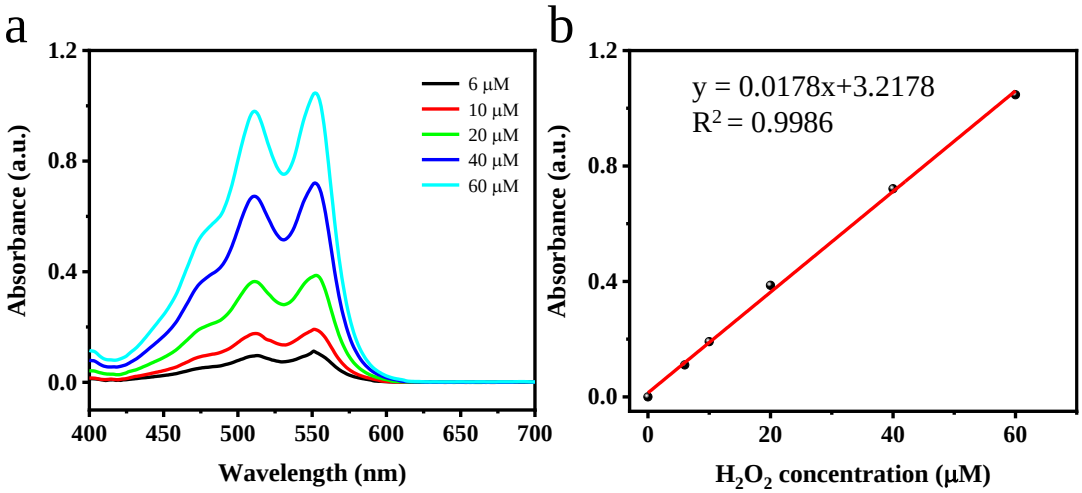

Figure S19 (a) The absorption spectra of H_2O_2 at different concentrations (6 μM, 10 μM, 20 μM, 40 μM, 60 μM) at wavelengths of 400-700 nm; (b) and a standard curve of H_2O_2 concentration-absorbance was drawn.

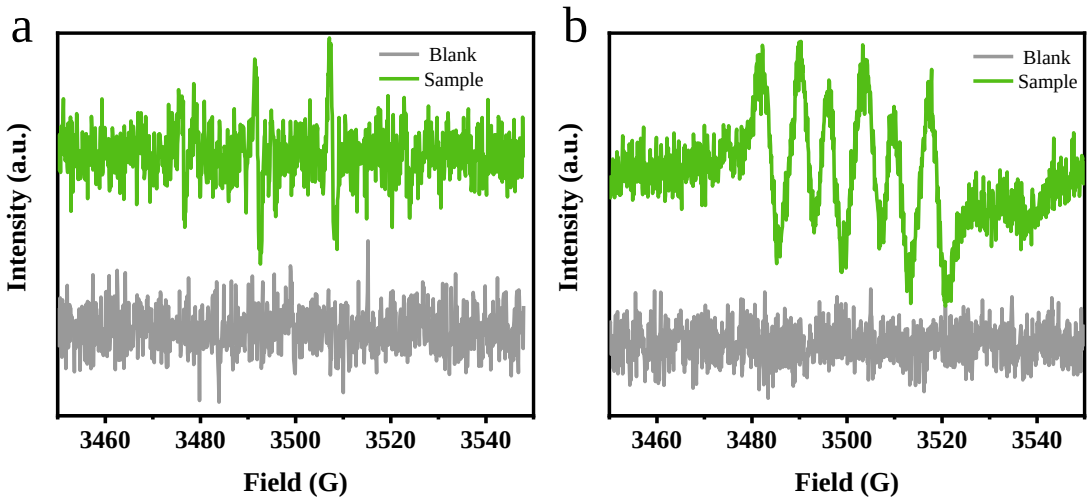

Figure S20. (a) ESR spectrum of DMPO-•OH and (b) DMPO-•OOH of the sample solution composed of 0.1 M KOH aqueous solution with 0.03 mM $FeSO_4$ and 10 mM H_2O_2, and blank contrast composed of 0.1 M KOH aqueous solution with 10 mM H_2O_2 (non Fe species added). The signals were collected after the radical trap (5,5-dimethyl-1-pyrroline-N-oxide, DMPO) added for 30 min.

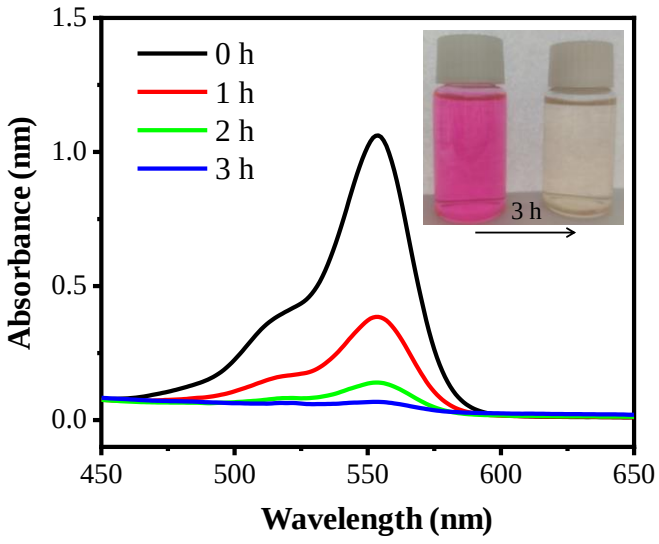

Figure S21. The degradation of Rhodamine B (RhB) via Fenton-like reactions. The primary solution is composed of 0.1 M KOH aqueous solution with 0.03 mM $FeSO_4$, 10 mM H_2O_2 and 10 mg/L RhB.

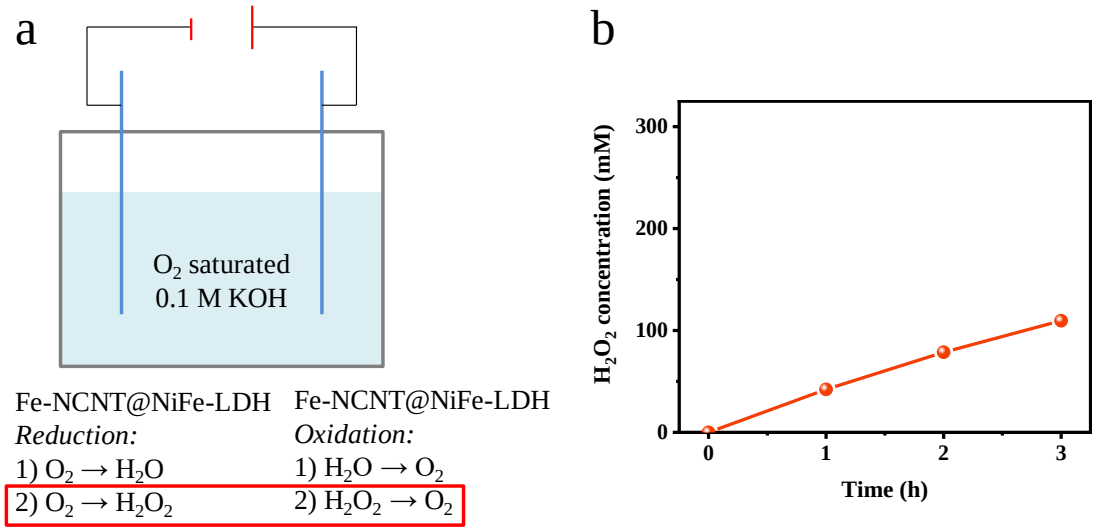

372

373 **Figure S22.** (a) A designed cell for simulating H_2O_2 generation in ORR and

374 electrochemical consumption in POR. (b) The H_2O_2 concentration varied along with

375 time. Conditions: The area of two electrodes (CFP/Fe-NCNT@NiFe-LDH) are of 2 cm^2,

376 the volume of the electrolyte is of 130 mL, and the discharging current is 10 mA.

377

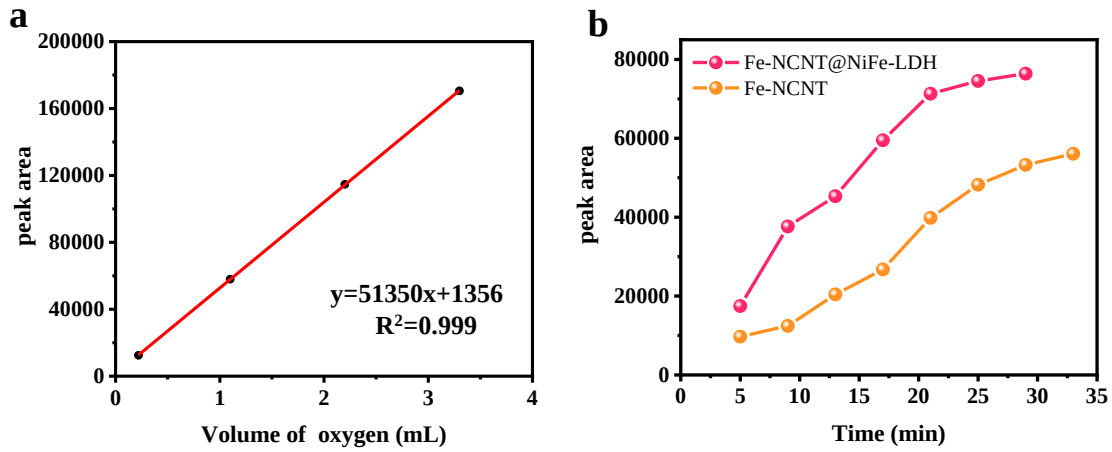

378

379 **Figure S23.** (a) Gas phase standard curve of oxygen, measured by gas chromatograph.

380 (b) Oxygen peak area at different times of Fe-NCNT@NiFe-LDH and Fe-NCNT.

381

382

383

Notes: Movies S3 (The isproportionation of H_2O_2 in NiFe-LDH contained H_2O_2-DI water system)**, S4** (The isproportionation of H_2O_2 in Fe-NCNT contained H_2O_2-DI water system)**, S5** (The isproportionation of H_2O_2 in Fe-NCNT@NiFe-LDH contained H_2O_2-DI water system), and **S6** (The isproportionation of H_2O_2 in Fe-NCNT@NiFe-LDH contained H_2O_2-1 M KOH-DI water system) are separately uploaded as MP4 files.

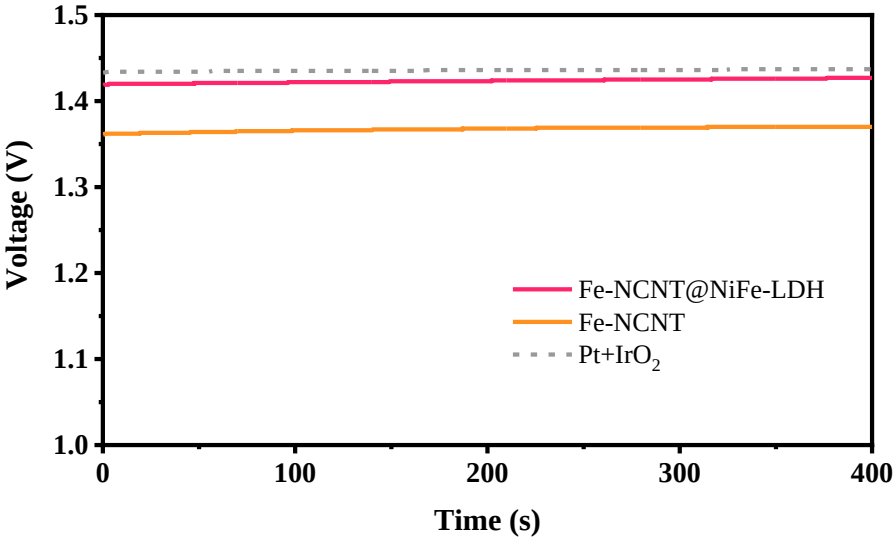

Figure S24. Open circuit curves of Fe-NCNT@NiFe-LDH, Fe-NCNT, and Pt+IrO_2 respectively assembled ZABs.

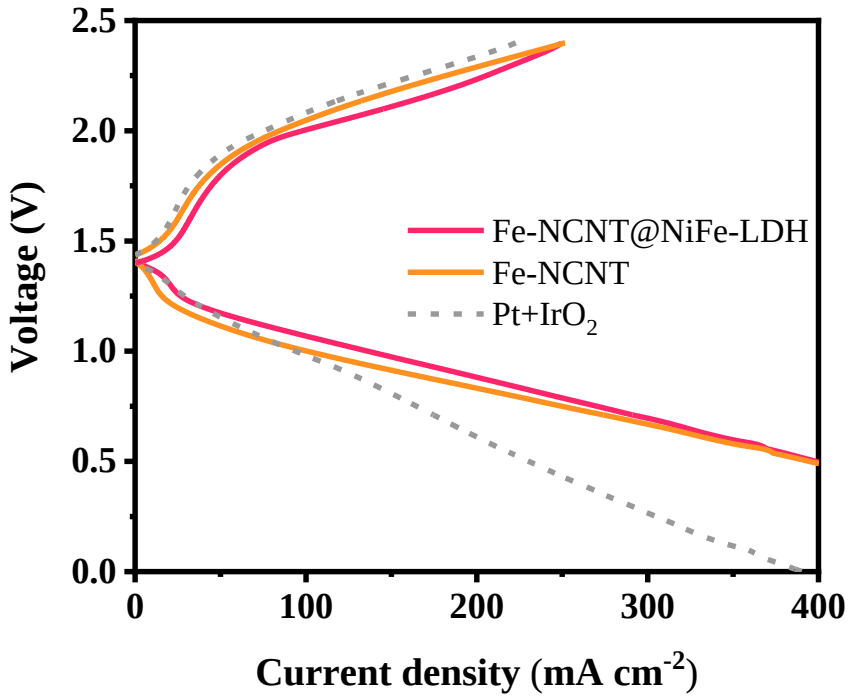

Figure S25. Discharge-charge polarization curves of Fe-NCNT@NiFe-LDH, Fe-NCNT, and Pt+IrO_2 respectively assembled ZABs.

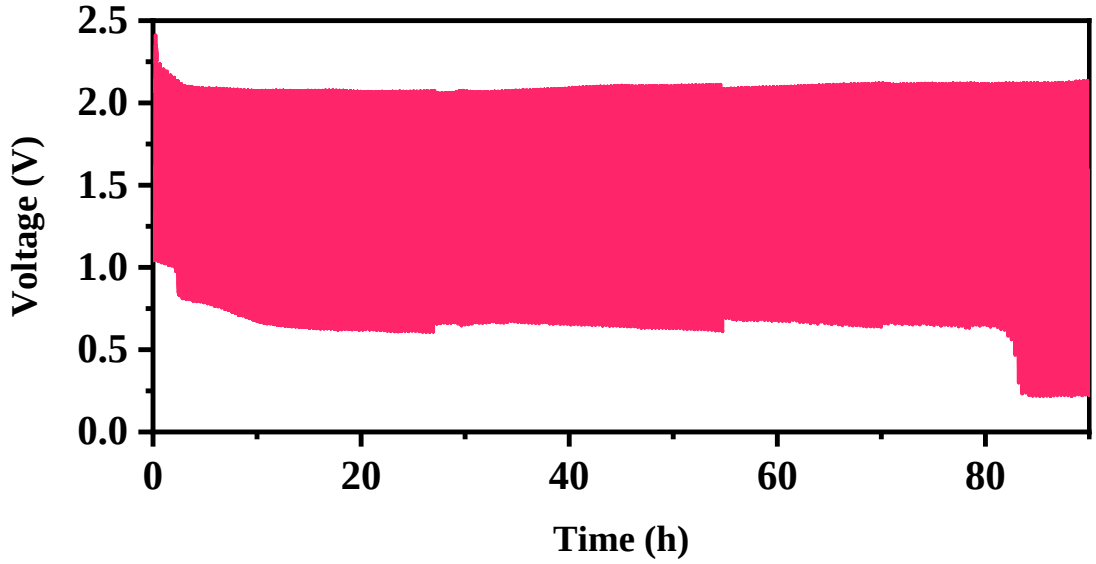

Figure S26. Charge/discharge cycle test at 100 mA cm^{-2} current density for Fe-NCNT@NiFe-LDH based ZAB.

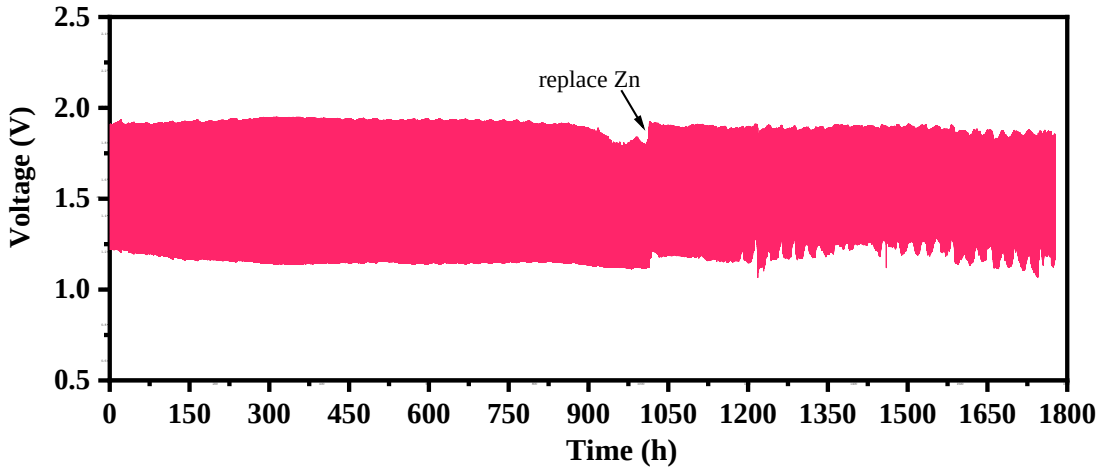

Figure S27. Charge/discharge cycle test at 10 mA cm^{-2} current density for Fe-NCNT@NiFe-LDH based ZAB.

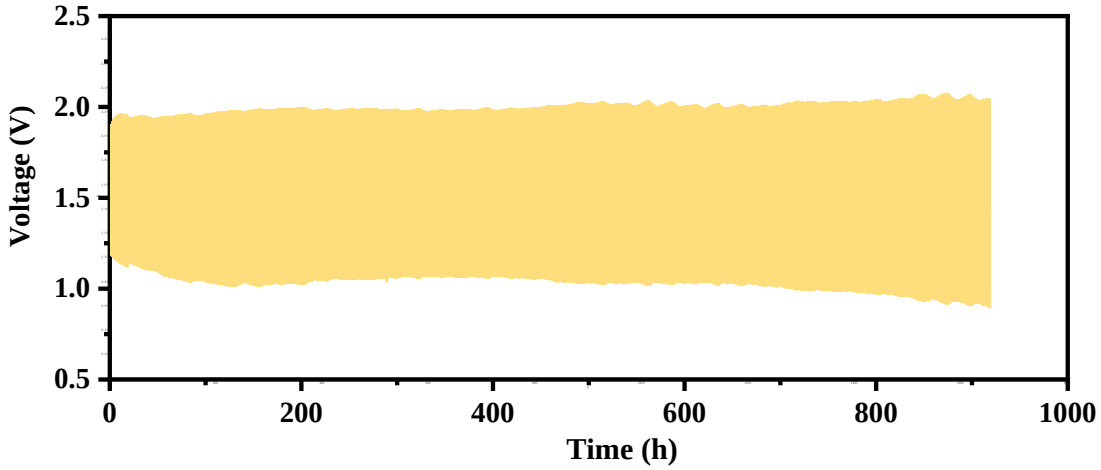

Figure S28. Charge/discharge cycle test at 10 mA cm^{-2} current density for Fe-NCNT based ZAB.

Tables

Table S1. Comparison of OER performance of Fe-NCNT@NiFe-LDH with recently reported electrocatalysts.[14-25]

Sample	OER			References
	$E_{j=10}$ (V)	$E_{j=100}$ (V)	Tafel slope (mV dec^{-1})	
Fe-NCNT@NiFe-LDH	**1.41**	**1.46**	**37**	**This work**
$FeCoSn(OH)_6$-300	1.50	1.55	39	14
$Ni_{83}Fe_{17}$-ONCAs	1.42	1.46	48	15
(Fe,Co)OOH/MI	1.46	1.52	53	16
CF-FeSO	1.42	1.46	40	17
Br-Ni-MOF (A)	1.54	1.71	79	18
W-$NiS_{0.5}Se_{0.5}$	1.40	1.47	41	19
a-LNFBPO	1.44	1.52	37	20
OLC-Co-N-C	1.57	1.66	58	21
Ir/CoNiB	1.41	1.47	35	22
ENWs-FeNi-C_2O_4	1.44	1.5	54	23
Co_3O_4-Mo_2N NFs	1.45	1.62	88	24
F-$Ni_{27}Fe_{10}$ LDH	1.46	1.48	29.7	25

Table S2. OER and ORR electrochemical performances of Fe-NCNT@NiFe-LDH, Fe-NCNT, and NiFe-LDH in 1 M KOH.

Sample	OER			ORR	ΔE
	η_{10} (mV)	η_{100} (mV)	Tafel slope (mV dec^{-1})	$E_{1/2}$ (V)	$E_{j=10}$-$E_{1/2}$ (V)
Fe-NCNT@NiFe-LDH	**180**	**230**	**37**	**0.87**	**0.54**
NiFe-LDH	250	300	39	0.78	0.70
Fe-NCNT	230	410	143	0.85	0.61

Table S3. OER and ORR electrochemical performances of Fe-NCNT@NiFe-LDH, Fe-NCNT, and NiFe-LDH in 0.1 M KOH.

Sample	OER		ORR	ΔE
	η_{10} (mV)	Tafel slope (mV dec^{-1})	$E_{1/2}$ (V)	$E_{j=10}$-$E_{1/2}$ (V)
Fe-NCNT@NiFe-LDH	**210**	**49**	**0.89**	**0.55**
NiFe-LDH	260	57	0.69	0.80
Fe-NCNT	250	185	0.88	0.60

Table S4 Comparison of overpotential difference ($\Delta E = E_{j=10} - E_{1/2}$) and ZAB (two-electrode cell) performance of (or based on) Fe-NCNT@NiFe-LDH with recently reported electrocatalysts. [25-62]

Sample	OER-ORR			ZABs		References
	ΔE (V)	$E_{j=10}$ (V)	$E_{1/2}$ (V)	Power density (mW cm^{-2})	cycling ability X h / Y cycle @ Z mA cm^{-2}	
Fe-NCNT@NiFe-LDH	**0.52**	**1.41**	**0.89**	**204**	**1743 h / 5229 cycle @ 50** **1777 h / 5331 cycle @ 10** **80 h / 240 cycle @ 100**	**This work**
FeNC|| F-$Ni_{27}Fe_{10}$ LDH||Zn(0.2 mm)	0.53	1.43	0.90	259	258 h @ 10	25
CoNC@LDH	0.63	1.47	0.84	173	3600cycle@10 656 cycle@50 29 cycle@100	26
Co SA/NCFs	0.76	1.61	0.85	154	600 h @ 10	27
Fe_2Ni_3-NFCM	0.69	1.51	0.82	128	10 h @ 10	28
Co-NC@LDH	0.80	1.6	0.8	107	300 h @ 5	29
FeNi@NCSs	0.71	1.55	0.84	128	120 h @ 5	30
Mn-RuO_2	0.64	1.5	0.86	181	2500 h @ 10 467 h @ 50 300 h @ 100	31
NiFe-LDH/FeSoy-CNSs-A	0.62	1.53	0.91	238	50 h @ 5	32
FeNi/N−LCN	0.72	1.57	0.85	162	1100 h @ 5 600 h @ 10	33
glu-NiFe	0.82	1.67	0.85	127	240 h @ 5	34
NiFe/N-CNT	0.77	1.52	0.75	300	300 cycle @ 5	35

NiFe-ND/FeCo-NC	0.81	1.66	0.85	141	160 h @ 20	36
Fe–Me–Ni	0.70	1.54	0.84	168	102 h @ 10	37
defected-NiFe LDH	0.72	1.47	0.75	35	100 cycle@ 10	38
$NiCo_2S_4$@NiFe LDH	0.67	1.50	0.83	--	--	39
DBD-NiFe/$NiSe_2$@NCNT	0.71	1.52	0.81	132	1000 cycle@10	40
NiFe@N-CFs	0.7	1.53	0.83	102	480 h @ 10 330 h @ 20	41
S-Ni_3FeN/NSG	0.61	1.49	0.88	207	1200 cycle@10	42
NiFe-Mi-C-Gr	0.68	1.54	0.85	111	100 h @ 10	43
NiFe@C@Co CNFs	0.70	1.57	0.87	130	200 h @ 5	44
NiFe-DG	0.73	1.59	0.86	148	12 h @ 10	45
NiFe@NCNT	0.77	1.56	0.79	360	200 h @ 10	46
NiFe LDH@Fe-N-CNFs	0.86	1.58	0.72	158	185 h @ 10	47
LDH@N-CoOx@C	0.66	1.50	0.84	156	150 h @ 5	48
ZGNiFe@NG	0.84	1.65	0.81	140	120 h @ 5	49
$NiFe_3$@NGHSNCNTs	0.79	1.61	0.82	126	1000 cycle@10	50
FeCo-NPCNs	0.6	1.47	0.87	161	400 cycle@10	51
Co_9S_8@Co/Mn-S,N-PC	0.7	1.55	0.85	80	210 h @ 10	52
FeNx/NC-S	0.63	1.55	0.92	194	65 h @ 10	53
Co@NrC-0.3	0.76	1.61	0.85	168	40 h @ 2	54
Co@N-HPC-800	0.87	1.69	0.82	89	25 h @ 5	55
Co@$CoFe_{0.01}$-N-C	0.81	1.65	0.84	174	100 h @ 1	56
BN-PCN	0.87	1.71	0.84	194	1000 h @ 5	57

o-$CoSe_2$/AK	0.77	1.61	0.84	122	90 h @ 5	58
NG/Ni	0.63	1.49	0.86	165	2500 h @ 2	59
CoWCP-NPC-2:1	0.63	1.43	0.80	205	83.5 h / 501 cycle @ 10	60
CoS/Co/MoC-N,S-PCNFs	0.65	1.52	0.87	169	50 h @ 2	61
Ti_3C_2@$SrTiO_3$	0.65	1.43	0.78	122	500 h@10	62

The ΔE values of catalysts containing NiFe nanosheets are concentrated in the range of 0.6−0.75 V, such as NiFe-LDH/FeSoy-CNSs-A[32] with a ΔE of 0.62 V ($E_{1/2}$ of 0.91 V and $E_{j=10}$ of 1.53 V), CoNC@LDH[26] with a ΔE of 0.63 V ($E_{1/2}$ of 0.84 V and $E_{j=10}$ of 1.47 V), $NiCo_2S_4$@NiFe-LDH[39] with ΔE of 0.63 V ($E_{1/2}$ of 0.83 V and $E_{j=10}$ of 1.497 V), and LDH@N-CoOx@C[48] with ΔE of 0.665 V ($E_{1/2}$ of 0.83 V and $E_{j=10}$ of 1.503 V). The ΔE of catalysts containing NiFe nanoparticles are principally concentrated in the scope of 0.7−0.85 V, such as Fe–Me–Ni[37] with ΔE of 0.702 V ($E_{1/2}$ of 0.841 V and $E_{j=10}$ of 1.543 V), NiFe@C@Co-CNFs[44] with ΔE of 0.7 V ($E_{1/2}$ of 0.87 V and $E_{j=10}$ of 1.57 V), NiFe@NCNTs[46] with ΔE of 0.77 V ($E_{1/2}$ of 0.79 V and $E_{j=10}$ of 1.56 V), and ZGNiFe@NG[49] with ΔE of 0.84 V ($E_{1/2}$ of 0.81 V and $E_{j=10}$ of 1.65 V).

References

1 H. Cai, X. Li, D. Ma, Q. Feng, D. Wang, Z. Liu, X. Wei, K. Chen, H. Lin, S. Qin and F. Lu, *Sci. Total. Environ.*, 2021, **764**, 144200.

2 N. D. Mohamad, Z. M. Zaki and A. Amir, *J. Environ. Chem. Eng.*, 2022, **10**, 107787.

3 Q. Zhang, P. Kumar, X. Zhu, R. Daiyan, N. M. Bedford, K. H. Wu, Z. Han, T. Zhang, R. Amal and X. Lu, *Adv. Energy Mater.*, 2021, **11**, 2100303.

4 H. Xie, X. Xie, G. Hu, V. Prabhakaran, S. Saha, L. Gonzalez-Lopez, A. H. Phakatkar, M. Hong, M. Wu, R. Shahbazian-Yassar, V. Ramani, M. I. Al-Sheikhly, D. Jiang, Y. Shao and L. Hu, *Nature Energy*, 2022, **7**, 281-289.

5 K. Ehelebe, D. Seeberger, M. T. Y. Paul, S. Thiele, K. J. J. Mayrhofer and S. Cherevko, *J. Electrochem. Soc.*, 2019, **166**, F1259-F1268.

6 M. Inaba, A. W. Jensen, G. W. Sievers, M. Escudero-Escribano, A. Zana and M. Arenz, *Energy Environ. Sci.*, 2018, **11**, 988-994.

7 J. Liu, Z. Gong, C. Allen, W. Ge, H. Gong, J. Liao, J. Liu, K. Huang, M. Yan, R. Liu, G. He, J. Dong, G. Ye and H. Fei, *Chem Catal.*, 2021, **1**, 1291-1307.

8 J. Wang, Z. Shu, Z. Chen, J. Su and C. Liu, *J. Clean Prod.*, 2022, **337**, 130489.

9 G. I. Berglund, G. H. Carlsson, A. T. Smith, H. Szöke, A. Henriksen and J. Hajdu, *Nature*, 2002, **417**, 463-468.

10 Y. Liu, Z. Li, F. Fan, X. Zhu, L. Jia, M. Chen, P. Du, L. Yang and S. Yang, *Adv. Sci.*, 2021, **8**, 2102422.

11 N. Ye, D. Zhang, Y. Yang, R. Wan, X. Peng, S. Chen, Q. Zhan and R. He, *Solid State Ionics.*, 2021, **362**, 115582.

12 B. Yan, Z. Shi, J. Lin, L. Zhang, L. Han, X. Shi and Q. Yang, *Environ. Sci. Nano*, 2022, **9**, 532-541.

13 M. Kou, Y. Wang, Y. Xu, L. Ye, Y. Huang, B. Jia, H. Li, J. Ren, Y. Deng, J. Chen, Y. Zhou, K. Lei, L. Wang, W. Liu, H. Huang and T. Ma, *Angew. Chem. Int. Ed.*,

2022, **61**, e202200413.

14 S. Liu, S. Geng, L. Li, Y. Zhang, G. Ren, B. Huang, Z. Hu, J. F. Lee, Y. H. Lai, Y. H. Chu, Y. Xu, Q. Shao and X. Huang, *Nat. Commun.*, 2022, **13**, 1187.

15 P. Liu, B. Chen, C. Liang, W. Yao, Y. Cui, S. Hu, P. Zou, H. Zhang, H. J. Fan and C. Yang, *Adv. Mater.*, 2021, **33**, 2007377.

16 W. Huang, J. Li, X. Liao, R. Lu, C. Ling, X. Liu, J. Meng, L. Qu, M. Lin, X. Hong, X. Zhou, S. Liu, Y. Zhao, L. Zhou and L. Mai, *Adv. Mater.*, 2022, **34**, 2200270.

17 W. H. Lee, M. H. Han, Y. J. Ko, B. K. Min, K. H. Chae and H. S. Oh, *Nat. Commun.*, 2022, **13**, 605.

18 W. Cheng, S. Xi, Z. P. Wu, D. Luan and X. W. Lou, *Sci. Adv.*, 2021, **7**, eabk0919.

19 Y. Wang, X. Li, M. Zhang, J. Zhang, Z. Chen, X. Zheng, Z. Tian, N. Zhao, X. Han, K. Zaghib, Y. Wang, Y. Deng and W. Hu, *Adv. Mater.*, 2022, **34**, 2107053.

20 J. Kwon, H. Han, S. Jo, S. Choi, K. Y. Chung, G. Ali, K. Park, U. Paik and T. Song, *Adv. Energy Mater.*, 2021, **11**, 2100624.

21 Z. Liang, N. Kong, C. Yang, W. Zhang, H. Zheng, H. Lin and R. Cao, *Angew. Chem. Int. Ed.*, 2021, **60**, 12759-12764.

22 C. Wang, P. Zhai, M. Xia, Y. Wu, B. Zhang, Z. Li, L. Ran, J. Gao, X. Zhang, Z. Fan, L. Sun and J. Hou, *Angew. Chem. Int. Ed.*, 2021, **60**, 27126-27134.

23 X. Qiao, H. Kang, Y. Li, K. Cui, X. Jia, X. Wu and W. Qin, *Small*, 2022, **18**, 2106378.

24 T. Wang, P. Wang, W. Zang, X. Li, D. Chen, Z. Kou, S. Mu and J. Wang, *Adv. Funct. Mater.*, 2021, **32**, 2107382.

503 25 X. Zhong, Y. Shao, B. Chen, C. Li, J. Sheng, X. Xiao, B. Xu, J. Li, H. M. Cheng
504 and G. Zhou, *Adv. Mater.*, 2023, 2301952.
505 26 C. X. Zhao, J. N. Liu, J. Wang, D. Ren, J. Yu, X. Chen, B. Q. Li and Q. Zhang,
506 *Adv. Mater.*, 2021, **33**, 2008606.
507 27 Y. Han, H. Duan, C. Zhou, H. Meng, Q. Jiang, B. Wang, W. Yan and R. Zhang,
508 *Nano Lett.*, 2022, **22**, 2497-2505.
509 28 T. Wang, Y. Han, P. Xu, X. Feng, W. Ji and H. Arandiyan, *Available at SSRN*, 2022.
510 29 D. Chen, X. Chen, Z. Cui, G. Li, B. Han, Q. Zhang, J. Sui, H. Dong, J. Yu and L.
511 Yu, *Chem. Eng. J.*, 2020, **399**, 125718.
512 30 S. Y. Lin, X. Zhang, S. Y. Sang, L. Zhang, J. J. Feng, A. Wang, Science, *J. Colloid.*
513 *Interf. Sci.*, 2022, **628**, 499.
514 31 C. Zhou, X. Chen, S. Liu, Y. Han, H. Meng, Q. Jiang, S. Zhao, F. Wei, J. Sun, T.
515 Tan and R. Zhang, *J. Am. Chem. Soc.*, 2022, **144**, 2694-2704.
516 32 M. Zhang, J. Zhang, S. Ran, L. Qiu, W. Sun, Y. Yu, J. Chen and Z. Zhu, *Nano Res.*,
517 2020, **14**, 1175-1186.
518 33 X. Li, Y. Liu, H. Chen, M. Yang, D. Yang, H. Li and Z. Lin, *Nano Lett.*, 2021, **21**,
519 3098-3105.
520 34 X. Chen, D. Chen, G. Li, P. Sha, J. Yu, L. Yu and L. Dong, *Electrochim. Acta,*
521 2022, **428**, 140938.
522 35 H. Lei, Z. Wang, F. Yang, X. Huang, J. Liu, Y. Liang, J. Xie, M. S. Javed, X. Lu,
523 S. Tan and W. Mai, *Nano Energy*, 2020, **68**, 104293.
524 36 Y. Wang, G. Zhang, M. Ma, Y. Ma, J. Huang, C. Chen, Y. Zhang, X. Sun and Z.

525 Yan, *Sci. China Mater.*, 2020, **63**, 1182-1195.

526 37 Y. Tang, Y. Lei, G. Li, T. Fu, Y. Xiang, J. Sha, H. Yang, P. Yu, Y. Si and C. Guo, *J.*

527 *Mater. Chem. A*, 2022, **10**, 5305-5316.

528 38 O. Ambriz-Peláez, J. Béjar, C. M. Ramos-Castillo, M. Guerra-Balcázar, L.

529 Álvarez-Contreras and N. Arjona, *Appl. Surf. Sci.*, 2022, **601**, 1154253.

530 39 X. Feng, Q. Jiao, W. Chen, Y. Dang, Z. Dai, S. L. Suib, J. Zhang, Y. Zhao, H. Li

531 and C. Feng, *Appl. Catal. B: Environ.*, 2021, **286**, 119869.

532 40 T. Hu, Z. Jiang, Z. Fu and Z. Jiang, *J. Mater. Chem. A*, 2022, **10**, 8739-8750.

533 41 Y. Niu, X. Teng, S. Gong and Z. Chen, *J. Mater. Chem. A*, 2020, **8**, 13725-13734.

534 42 C. Lai, M. Gong, Y. Zhou, J. Fang, L. Huang, Z. Deng, X. Liu, T. Zhao, R. Lin, K.

535 Wang, K. Jiang, H. Xin and D. Wang, *Appl. Catal. B: Environ.*, 2020, **274**, 119086.

536 43 Y. Xiang, C. Xu, T. Fu, Y. Tang, G. Li, Z. Xiong, C. Guo and Y. Si, *Appl. Surf. Sci.*,

537 2022, **575**, 151730.

538 44 X. Chen, J. Pu, X. Hu, Y. Yao, Y. Dou, J. Jiang and W. Zhang, *Small*, 2022, **18**,

539 2200578.

540 45 K. Khan, X. Yan, Q. Yu, S. H. Bae, J. J. White, J. Liu, T. Liu, C. Sun, J. Kim and

541 H. M. Cheng, *Nano Energy*, 2021, **90**, 106488.

542 46 M. Jiang, Z. Tan and M. Cao, *Int. J. Hydrogen Energy*, 2021, **46**, 15507-15516.

543 47 D. Wu, X. Hu, Z. Yang, T. Yang, J. Wen, G. Lu, Q. Zhao, Z. Li, X. Jiang and C.

544 Xu, *Ind. Eng. Chem. Res.*, 2022, **61**, 7523-7528.

545 48 Y. Hao, Y. Kang, H. Kang, H. Xin, F. Liu, L. Li, W. Wang and Z. Lei, *J. Power*

546 *Sources*, 2022, **524**, 231076.

547 49 W. Li, Y. Wu, M. Chen, P. Dai, T. Jiang and S. Zhou, *J. Alloy. Compd*, 2022, **925**,
548 166658.
549 50 Y. Ma, W. Chen, Z. Jiang, X. Tian, X. WangGuo, G. Chen and Z.-J. Jiang, *J. Mater.*
550 *Chem. A*, 2022, **10**, 12616-12631.
551 51 L. Lin, P. Xue, X. Cui, J. Liu, J. Liu, M. Tang and Z. Wang, *J. Alloy Compd.*, 2022,
552 **909**, 164625.
553 52 R. M. Sun, L. Zhang, J. J. Feng, K. M. Fang and A. J. Wang, *J. Colloid Interf. Sci.*,
554 2022, **608**, 2100-2110.
555 53 L. Wu, R. Zhao, G. Du, H. Wang, M. Hou, W. Zhang, P. Sun and T. Chen, *Green*
556 *Energy Environ.*, 2022, DOI: 10.1016/j.gee.2022.03.014.
557 54 J. Yu, Y. Dai, Z. Zhang, T. Liu, S. Zhao, C. Cheng, P. Tan, Z. Shao and M. Ni,
558 *Carbon Energy*, 2022, **4**, 576-585.
559 55 Y. Liu, Z. Chen, N. Zhao, G. Tong, Z. Li, B. Wang, Y. Du, Q. Pan, Z. Li and Y.
560 Xie, *Chem. Eng. J.*, 2022, **433**, 134469.
561 56 R. Hao, J. Chen, Z. Wang, Y. Huang, P. Liu, J. Yan, K. Liu, C. Liu and Z. Lu, *J.*
562 *Colloid Interf. Sci.*, 2021, **586**, 621-629.
563 57 Y. Kang, W. Wang, J. Li, S. Imhanria, Y. Hao and Z. Lei, *J. Power Sources*, 2021,
564 **493**, 229665.
565 58 P. Liu, G. Cheng, G. Liu, M. Sun, S. Fu, Z. Zhou, S. Han and L. Yu, *J. Mater. Sci.*
566 *Mater. in El.*, 2021, **32**, 14385-14397.
567 59 Y. Zhang, X. P. Kong, X. Lin, K. Hu, W. Zhao, G. Xie, X. Lin, X. Liu, Y. Ito and
568 H. J. Qiu, *J. Energy Chem.*, 2022, **66**, 466-473.

60 Y. Zhang, W. Shi, L. Bo, Y. Shen, X. Ji, L. Xia, X. Guan, Y. Wang and J. Tong, *Chem. Eng. J.*, 2022, **431**, 134188.

61 Y. Ren, H. Wang, T. Zhang, L. Ma, P. Ye, Y. Zhong and Y. Hu, *Chinese Chem. Lett.*, 2021, **32**, 2243-2248.

62 X. Hui, P. Zhang, Z. Wang, D. Zhao, Z. Li, Z. Zhang, C. Wang and L. Yin, *ACS Appl. Energy Mater.*, 2022, **5**, 6100-6109.